



Cite this: *RSC Adv.*, 2022, **12**, 30577

# Visible-light photoelectrocatalysis/ $\text{H}_2\text{O}_2$ synergistic degradation of organic pollutants by a magnetic $\text{Fe}_3\text{O}_4@\text{SiO}_2@\text{mesoporous TiO}_2$ catalyst-loaded photoelectrode<sup>†</sup>

Bo Zhang, Xuemei Li, \* Yongshan Ma, Tianyi Jiang, Yanyan Zhu and Huixue Ren

In this paper, we describe a method for photoelectrocatalysis (PEC)/ $\text{H}_2\text{O}_2$  synergistic degradation of organic pollutants with a magnetic  $\text{Fe}_3\text{O}_4@\text{SiO}_2@\text{mesoporous TiO}_2$  (FST) photocatalyst-loaded electrode. At optimal conditions of pH 3.0, 2.25%  $\text{H}_2\text{O}_2$ , working electrode (fixed FST 30 mg) potential +0.6 V (vs. SCE), and 10 mg L<sup>-1</sup> of all experimental pollutants, the FST PEC/ $\text{H}_2\text{O}_2$  synergistic system exhibited high activity and stability for the removal of various organic pollutants under visible light with comparable degradation efficiencies, including MB (98.8%), rhodamine B (Rh B, 96.7%), methyl orange (MO, 97.7%), amoxicillin (AMX, 83.9%). Moreover, this system obtained TOC removal ratios of 83.5% (MB), 77.9% (Rh B), 80.2% (MO), 65.5% (AMX) within 8 min. The kinetic rate constants of the PEC/ $\text{H}_2\text{O}_2$  synergistic system were nearly 53 and 1436 times higher than that of the PEC process and  $\text{H}_2\text{O}_2$  photolysis under visible light, respectively. Furthermore, the main reactive oxidant species ( $\cdot\text{OH}$ ,  $\cdot\text{O}_2^-$ ) were studied and enhanced mechanisms of the photocatalytic-electro- $\text{H}_2\text{O}_2$  coupling system were proposed. This work brings new insights to efficiently purify organic pollutants by PEC coupled with peroxide under solar light illumination.

Received 18th August 2022  
 Accepted 21st October 2022

DOI: 10.1039/d2ra05183d  
[rsc.li/rsc-advances](http://rsc.li/rsc-advances)

## 1. Introduction

With advances in industrialization and rapid population growth, organic pollutants are frequently detected in water environments. They continue to be enriched in food chains and food webs, endangering ecological environments and human health.<sup>1</sup> These organic pollutants cannot be completely eliminated by wastewater treatment processes, resulting in residues in groundwater and surface water. Therefore, it is necessary to develop suitable technological approaches for the decomposition and mineralization of refractory organic pollutants and removal of refractory organic pollutants from water environments.

Refractory organic pollutants cannot be effectively degraded and mineralized by using the conventional biological, physical and chemical wastewater treatment methods. Compared to these traditional technologies, advanced oxidation processes (AOPs) have many advantages with regards to degrading refractory organic pollutants, which include complete mineralization and oxidation of refractory organic pollutants, low secondary pollution outcomes, and small working area. AOPs

such as heterogeneous catalysis,<sup>2</sup> photoelectrocatalysis (PEC),<sup>3</sup> photocatalysis,<sup>4</sup> Fenton<sup>5</sup> and Fenton-like,<sup>6</sup> electro-Fenton and photoelectro-Fenton,<sup>7</sup> electrochemical oxidation,<sup>8</sup> etc. can be used for wastewater treatment. The PEC technology combines photocatalysis and electrochemical methods, which is an efficient process to remove recalcitrant organic pollutants from water.<sup>9</sup> Biasing the semiconductor photoanode with a voltage under illumination, photogenerated  $\text{h}^+-\text{e}^-$  pairs can be effectively inhibited by an external electric field, resulting in improved photocatalytic activities.<sup>10</sup> A lot of research has been done on the photoanode materials, reaction mechanisms and kinetics of PEC,<sup>11</sup> which shows that it is a promising wastewater treatment technology.

$\text{TiO}_2$  is considered as a promising photocatalyst for wastewater treatment<sup>12</sup> due to its unique photoelectric performance and high photochemical stability, and it has been widely exploited as photoanode material in PEC systems.<sup>13</sup> However, due to the large forbidden bandwidth of  $\text{TiO}_2$  (3.2 eV for anatase type), it can only absorb ultraviolet light ( $\lambda \leq 387$  nm), which limits its photocatalytic activity under visible light.<sup>14</sup> In addition, photogenerated hole-electron pairs ( $\text{h}^+-\text{e}^-$ ) of  $\text{TiO}_2$  can rapidly recombine, resulting in low catalytic efficiency.<sup>15</sup> So there have been many attempts to modify titanium dioxide (e.g. dye sensitization, metal/non-metal doping, morphology control, and composite photocatalysts) to overcome aforesaid challenges.<sup>16</sup> Among the composite photocatalysts, magnetic

School of Municipal and Environmental Engineering, Shandong Jianzhu University, Jinan 250101, Shandong, China. E-mail: [ch1889l@sdu.edu.cn](mailto:ch1889l@sdu.edu.cn)

† Electronic supplementary information (ESI) available. See DOI: <https://doi.org/10.1039/d2ra05183d>



**TiO<sub>2</sub>** is not only to be separated and recovered from reaction mixtures easily, but also contains some magnetic nanoparticles that have good visible-light absorption and excellent optical/electrical properties, further improving the degradation kinetics of pollutants.<sup>17</sup> Due to its low toxicity, biocompatibility, and superparamagnetism, magnetite (Fe<sub>3</sub>O<sub>4</sub>) has become one of the most widely used magnetic nanoparticles<sup>18,19</sup> in the fabrication of magnetic TiO<sub>2</sub> photocatalysts. Previous studies have shown that direct contact of the magnetic core with photocatalysts leads to photodissolution of Fe<sub>3</sub>O<sub>4</sub>,<sup>20</sup> as well as increases recombination of photogenerated charge carriers, thereby reducing the catalytic activity.<sup>21</sup> It has been reported that the SiO<sub>2</sub> interlayer between TiO<sub>2</sub> and the magnetic core can effectively prevent the chemical- and photo-dissolution of Fe<sub>3</sub>O<sub>4</sub><sup>22,23</sup> and can improve the photocatalytic activity of TiO<sub>2</sub>.<sup>24</sup> And because of silica's well-known special characteristics, such as low cost, thermal and mechanical stability, surface chemical and adsorption capacity, and optical transparency in the wavelength region where TiO<sub>2</sub> absorbs,<sup>25</sup> previous studies have shown that the core-shell SiO<sub>2</sub>@TiO<sub>2</sub> has excellent photocatalytic efficiency for the pollutant degradation than pure TiO<sub>2</sub>.<sup>26</sup> In recent years, the research on magnetic TiO<sub>2</sub> composite photocatalysts based on Fe<sub>3</sub>O<sub>4</sub> has mostly focused on the application of Fe<sub>3</sub>O<sub>4</sub>@SiO<sub>2</sub>@TiO<sub>2</sub> in photocatalysis.<sup>27-33</sup> The role of Fe<sub>3</sub>O<sub>4</sub> in these studies is primarily in the area of magnetic separation, but less attention is paid to how to improve TiO<sub>2</sub> photocatalytic activity. Meanwhile, less research has been conducted on Fe<sub>3</sub>O<sub>4</sub>@SiO<sub>2</sub>@TiO<sub>2</sub> in photoelectrocatalysis,<sup>34</sup> and few studies have comprehensively discussed the issues of expanding the light absorption range, increasing the photoelectrocatalytic activity, effective charge separation performance, and stable recyclability.<sup>35</sup> Therefore, it is necessary to further study the effect of Fe<sub>3</sub>O<sub>4</sub> on the band gap and optical absorption of Fe<sub>3</sub>O<sub>4</sub>@SiO<sub>2</sub>@TiO<sub>2</sub> composites, and on the optical and electrical properties of composite photoanodes. We successfully prepared a novel composite photoelectrocatalytic material (Fe<sub>3</sub>O<sub>4</sub>@SiO<sub>2</sub>@mesoporous TiO<sub>2</sub>, FST), encapsulated by layers of Fe<sub>3</sub>O<sub>4</sub>, SiO<sub>2</sub> and mesoporous TiO<sub>2</sub> particles with a unique core-shell structure. The dense SiO<sub>2</sub> layer prevents the magnetic core from interacting with TiO<sub>2</sub>, reducing the electron-hole recombination rate, and preventing photo-dissolution of Fe<sub>3</sub>O<sub>4</sub> (ref. <sup>36</sup>) and dissolution under acidic conditions. Fe<sub>3</sub>O<sub>4</sub> can lower the band gap of FST and enhance the visible-light absorption. Due to the mesoporous structure and anatase TiO<sub>2</sub> particles, FST has a high specific surface area and exceptional catalytic performance.

Because of mass transfer limitations and the low number of active radicals generated in the heterogeneous PEC systems, the efficiency of photoelectrocatalytic oxidation for pollutant removal should be increased. UV/H<sub>2</sub>O<sub>2</sub> systems have been applied to the degradation of various pollutants.<sup>37</sup> The addition of H<sub>2</sub>O<sub>2</sub> to other AOPs can improve the degradation efficiency of organic pollutants by strengthening the generation of radicals in a wider spectral range.<sup>38</sup> It has been reported that H<sub>2</sub>O<sub>2</sub> can enhance the generation of

radicals and improve the degradation efficiency in PEC systems.<sup>39,40</sup>

In this study, a PEC/H<sub>2</sub>O<sub>2</sub> coupling system with magnetic FST-loaded photoanode was constructed to discuss the synergistic degradation of organic pollutants. The FST PEC/H<sub>2</sub>O<sub>2</sub> system was effective for the degradation of methylene blue, rhodamine B, methyl Orange, and amoxicillin under visible light. With the addition of 2.25% H<sub>2</sub>O<sub>2</sub>, the reaction kinetic rate constant of the PEC/H<sub>2</sub>O<sub>2</sub> synergistic system was nearly 53 times that of individual PEC. In the PEC/H<sub>2</sub>O<sub>2</sub> process, 'O<sub>2</sub><sup>-</sup> and 'OH were generated to degrade pollutants, and at the same time, the photogenerated e<sup>-</sup> could be captured by a sufficient amount of H<sub>2</sub>O<sub>2</sub> to generate 'OH, which increased the amounts of strong oxidizing substances and promoted the separation of photogenerated h<sup>+</sup>-e<sup>-</sup>. The formed photocatalytic-electro-H<sub>2</sub>O<sub>2</sub> coupling system improved the degradation efficiency of diverse organic pollutants, and maintained the high degradation efficiency within 8 degradation cycles.

## 2. Experimental section

### 2.1. Materials and reagents

Indium tin oxide (ITO) coated glass slides (25 mm × 25 mm × 1.1 mm, 8–12 Ω sq<sup>-1</sup>) were purchased from Sigma-Aldrich (Shanghai Warehouse). Methylene blue (MB, C<sub>16</sub>H<sub>18</sub>ClN<sub>3</sub>S, ≥98%), rhodamine B (Rh B, C<sub>28</sub>H<sub>31</sub>ClN<sub>2</sub>O<sub>3</sub>, ≥99%), methyl orange (MO, C<sub>14</sub>H<sub>14</sub>N<sub>3</sub>NaO<sub>3</sub>S, 98%), amoxicillin (AMX, C<sub>16</sub>H<sub>19</sub>-N<sub>3</sub>O<sub>5</sub>S·3H<sub>2</sub>O, 98%), titanium butoxide (C<sub>16</sub>H<sub>36</sub>O<sub>4</sub>Ti, AR), poly(propylene glycol) (PPG 1000, H[OCH(CH<sub>3</sub>)CH<sub>2</sub>]<sub>n</sub>OH, average M<sub>n</sub> ~ 1000), tetraethyl orthosilicate (TEOS, C<sub>8</sub>H<sub>20</sub>O<sub>4</sub>Si, >99%), ethanol (CH<sub>3</sub>CH<sub>2</sub>OH, ≥99.5%) were purchased from Macklin Inc. (Shanghai, China). FeCl<sub>3</sub>·6H<sub>2</sub>O (AR), FeSO<sub>4</sub>·7H<sub>2</sub>O (AR), NH<sub>3</sub> H<sub>2</sub>O (AR, 28%), HCl (AR, 36%), glacial acetic acid (CH<sub>3</sub>-COOH, AR), and other inorganic metal salts were purchased from Sinopharm Chemical Reagent Co., Ltd (Shanghai, China). All solutions were prepared using ultrapure water from a Milli-Q water purification system (resistivity > 16 MΩ cm at 25 °C).

### 2.2. Fabrication of photoelectrode

The detailed synthesis of FST and TiO<sub>2</sub> can be found from ESI.†

**FST-loaded photoelectrode:** 30 mg FST was sonicated in 1 mL ethanol to obtain a 30 mg mL<sup>-1</sup> FST suspension. The ITO coated glass slides, which have been cleaned *via* ultrasonic waves in acetone, ethanol and distilled water, were connected to a section of electrode wires with conductive silver glue. The epoxy resin glue was used to seal the connection between ITO and the electrode wire. Then, 30 mg mL<sup>-1</sup> FST suspension was applied on the ITO work surface and dried at 25 °C. During the PEC/H<sub>2</sub>O<sub>2</sub> synergistic degradation experiment, the Nd-Fe-B (25 mm × 25 mm × 5 mm) magnet was coated with a layer of polyvinyl chloride film to avoid the contact of the Nd-Fe-B magnet with the reaction solution, and glued to the back of the ITO work surface.<sup>31</sup>

**TiO<sub>2</sub>-loaded photoelectrode:** 30 mg TiO<sub>2</sub> was sonicated in 1 mL ethanol to obtain a 30 mg mL<sup>-1</sup> TiO<sub>2</sub> suspension. Add the



TiO<sub>2</sub> suspension dropwise to the cleaned ITO conductive surface and dry at 25 °C.

### 2.3. Characterization of FST

Sample microscopic morphologies were investigated by field emission transmission electron microscopy (JEM-2100F, JEOL, Japan). The X-ray diffraction (XRD) pattern was measured by a Bruker X-ray diffractometer (D8 advance, Germany). X-ray photoelectron spectroscopy (XPS, ThermoEscalab 250Xi, Thermo fisher, USA) was performed to assess surface properties and composition. The UV-vis diffuse reflectance spectrum was determined by UV-visible-near infrared light spectrophotometry (Cary 5000, Agilent, USA). Mesoporous structures of catalysts were measured using the surface area and pore size analyzer (Autosorb-iQ, Quantachrome, USA). Magnetic data was obtained by an MPMS magnetic measurement system (MPMS-VSM, Quantum Design, USA).

### 2.4. The PEC/H<sub>2</sub>O<sub>2</sub> synergistic degradation experiment

Experiments were conducted in a quartz photoelectric reactor with the volume of 60 mL, and the light source was a xenon light source (H8X-F300, Beijing Newbit Technology Co., Ltd.). Potentiostat experiments were performed using a three electrode system consisting of a working electrode (W.E., FST + ITO photoelectrode, anode), a counter electrode (C.E., Pt electrode, cathode), and a reference electrode (R.E., saturated calomel electrode, recorded as SCE), which were controlled using a CHI electrochemical analyzer (CHI 760E, CH Instruments, Inc., USA). The distance between the working electrode and the light source was 10 cm. To enhance conductivity, 0.05 mol per L Na<sub>2</sub>SO<sub>4</sub> was added to the pollutants solution (the concentration was 10 mg L<sup>-1</sup>) as the supporting electrolyte.

The UV-vis spectrophotometer (UV-5800, Shanghai) was used to determine pollutant concentrations ( $\lambda_{\text{max,MB}} = 664$  nm,  $\lambda_{\text{max,Rh B}} = 554$  nm,  $\lambda_{\text{max,MO}} = 463$  nm,  $\lambda_{\text{max,AMX}} = 198$  nm). The total organic carbon (TOC) was determined using a TOC analyzer (Elementer, vario TOC).

## 3. Results and discussion

### 3.1. Morphology and structural analysis of catalysts

The FST microspheres were characterized by scanning transmission electron microscopy (STEM). The high-angle annular dark-field (HAADF) image in Fig. 1a exhibited an overlay of Fe<sub>3</sub>O<sub>4</sub> core and TiO<sub>2</sub> shell with a clear separation. A clear contrast difference was also observed in EDS mappings (Fig. 1b), confirming the core-shell structure of FST. The diameter of Fe<sub>3</sub>O<sub>4</sub> core was about 580 nm, while thickness of the SiO<sub>2</sub> intermediate layer and TiO<sub>2</sub> shell layer was about 45 nm and 50 nm, respectively.

FST, Fe<sub>3</sub>O<sub>4</sub>@SiO<sub>2</sub> and Fe<sub>3</sub>O<sub>4</sub> nanoparticles were analyzed by X-ray diffraction (XRD) (Fig. 2). Fe<sub>3</sub>O<sub>4</sub> nanoparticles exhibited characteristic peaks at  $2\theta = 30.1^\circ, 35.44^\circ, 43.2^\circ, 53.56^\circ, 57.1^\circ$  and  $62.6^\circ$ , in agreement with previously reported XRD patterns of Fe<sub>3</sub>O<sub>4</sub>.<sup>41</sup> The obtained material was Fe<sub>3</sub>O<sub>4</sub> crystal with an irregular octahedral inverse spinel structure. Fe<sub>3</sub>O<sub>4</sub>@SiO<sub>2</sub> particles exhibited comparable XRD patterns to Fe<sub>3</sub>O<sub>4</sub>, indicating that the Fe<sub>3</sub>O<sub>4</sub> crystal structure was well maintained. Characteristic peaks at  $25.4^\circ, 37.8^\circ, 48.1^\circ, 54.1^\circ, 55.2^\circ, 62.8^\circ$  and  $68.8^\circ$  of FST can be attributed to anatase TiO<sub>2</sub> (101), (004), (200), (105), (211), (204) and (116), respectively. The high crystallinity of nano-TiO<sub>2</sub> can reduce the migration distance of photogenerated charges, and accordingly reduce the recombination rate.<sup>42</sup>

The characterization data and analysis details of mesoporous structure, magnetic response and XPS spectrum were described in the ESI.†

### 3.2. Photo-electric performance

The UV-vis diffuse reflectance spectra (DRS) of Fe<sub>3</sub>O<sub>4</sub>, Fe<sub>3</sub>O<sub>4</sub>@SiO<sub>2</sub>, TiO<sub>2</sub> nanoparticles and FST were shown in Fig. 3a. TiO<sub>2</sub> exhibited a lower optical absorption response from 400–1000 nm. Comparing the optical absorption responses of Fe<sub>3</sub>O<sub>4</sub>, Fe<sub>3</sub>O<sub>4</sub>@SiO<sub>2</sub> and FST at 400–1000 nm, Fe<sub>3</sub>O<sub>4</sub> has the strongest light absorption, while FST has a weaker light absorption due to the encapsulation of SiO<sub>2</sub> and TiO<sub>2</sub>. However, the visible-NIR absorption of FST is still significantly enhanced compared

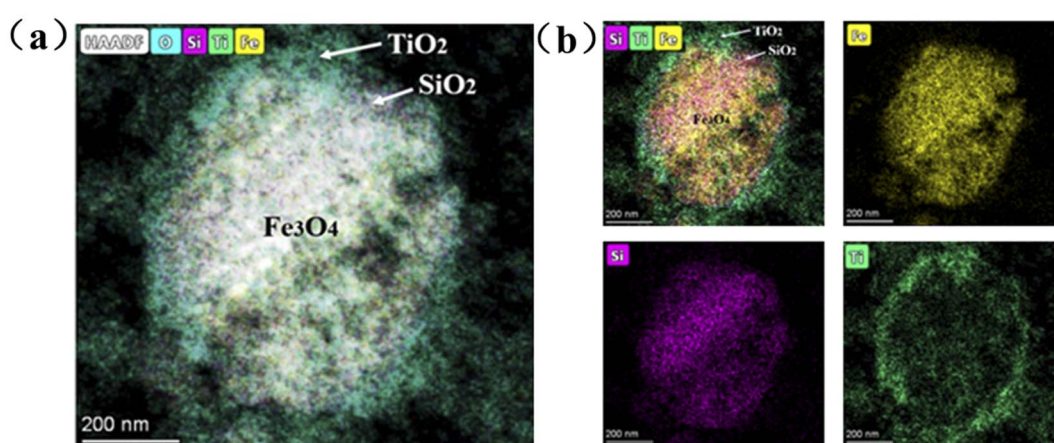


Fig. 1 Scanning transmission electron microscopy (STEM) of FST: (a) HAADF image, (b) EDS mappings of Fe<sub>3</sub>O<sub>4</sub>, SiO<sub>2</sub>, and TiO<sub>2</sub>.



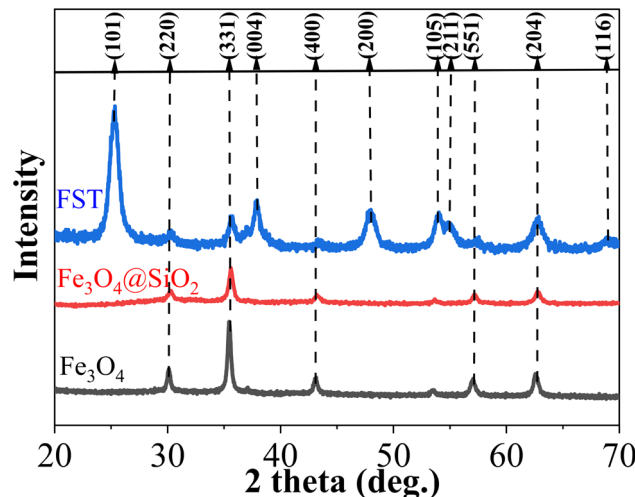


Fig. 2 X-ray diffraction (XRD) pattern.

with that of  $\text{TiO}_2$ . Since FST is very sensitive to visible light, it enhances the performance of visible-light driven photoelectrocatalytic systems. Using the Tauc equation (eqn (1)) and the Kubelka–Munk function (eqn (2)), band gaps of  $\text{Fe}_3\text{O}_4$ ,  $\text{Fe}_3\text{O}_4@\text{SiO}_2$ ,  $\text{TiO}_2$  and FST were calculated as previously reported.<sup>43</sup>

$$[F(R)h\nu]^{0.5} = A(h\nu - E_g) \quad (1)$$

$$F(R) = (1 - R)^2/2R \quad (2)$$

Fig. 3b shows that the effective  $E_g$  values of samples were calculated by plotting  $[F(R)h\nu]^{0.5}$  versus  $h\nu$ . The indirect  $E_g$  values of catalysts can be determined by extrapolating the linear part at  $[F(R)h\nu]^{0.5} = 0$ . The  $E_g$  values for  $\text{Fe}_3\text{O}_4$ ,  $\text{Fe}_3\text{O}_4@\text{SiO}_2$ , FST and  $\text{TiO}_2$  were 1.49, 1.77, 1.88 and 3.19 eV, respectively. The addition of  $\text{Fe}_3\text{O}_4$  and  $\text{SiO}_2$  reduced the forbidden bandwidth of  $\text{TiO}_2$ , so that the light absorption of FST extended to the visible light region. The higher photocatalytic performance at higher

wavelength has shown the capability to potentially utilize natural solar light as activation source.<sup>29</sup> Compared with other materials ( $\text{WO}_3$ ,  $\text{ZnO}$ ,  $\text{CdS}$ , etc.) with low  $E_g$  and activity in visible light, FST has lower  $E_g$ , and has the characteristics of nontoxicity, biochemical inertness, low cost of  $\text{TiO}_2$ .

To investigate the charge transfer of interface between photocatalysts and reaction solutions, Electrochemical Impedance Spectroscopy (EIS) was conducted. The EIS Nyquist plots were shown in Fig. 4a. The circular radius of ITO + FST was smaller than the pristine ITO and ITO +  $\text{TiO}_2$ . A smaller impedance arc radius at low frequencies signifies a lower charge transfer resistance ( $R_{ct}$ ),<sup>44</sup> thus,  $\text{h}^+ - \text{e}^-$  pairs are efficiently separated. In this regard, ITO + FST possessed faster charge transfer rate and more efficient separation of  $\text{h}^+ - \text{e}^-$  pairs than ITO and ITO +  $\text{TiO}_2$  at the solid–liquid interface.

The photocurrent of W.E. at +0.6 V (vs. SCE) was measured to test the separation efficiency of photogenerated charge by several on/off cycles of visible-light. Photocurrent response curves of pristine ITO, ITO +  $\text{TiO}_2$  and ITO + FST were shown in Fig. 4b. The photocurrents generated by ITO + FST, ITO and ITO +  $\text{TiO}_2$  photoelectrodes were 0.17, 0.10, and 0.07 mA, respectively. The photocurrent of the ITO + FST electrode was about 1.7-fold that of ITO electrode, and 2.4-fold that of ITO +  $\text{TiO}_2$  electrode, respectively. The photocurrent enhancement of ITO + FST induced by visible light indicates that the photogenerated  $\text{h}^+ - \text{e}^-$  pairs at the interface have higher separation efficiency and less recombination. The high separation rate of  $\text{h}^+ - \text{e}^-$  pairs can promote the movement and subsequent reaction of electrons. However,  $\text{TiO}_2$  had lower conductivity than ITO, and absorbed less visible-light, so the photocurrent of the ITO +  $\text{TiO}_2$  was lower than that of the pristine ITO.

### 3.3. Control experiments for different degradation methods

Taking MB as the model pollutant, the effects of direct photolysis (PO), photocatalysis (PC), electrocatalysis (EC), photoelectrocatalysis (PEC), and PEC/ $\text{H}_2\text{O}_2$  synergistic system on MB degradation were compared (Fig. 5). In the PO, PC, PEC, and PEC/ $\text{H}_2\text{O}_2$  synergistic system, illumination was the visible light provided by the xenon lamp light source. In the EC, PEC, and

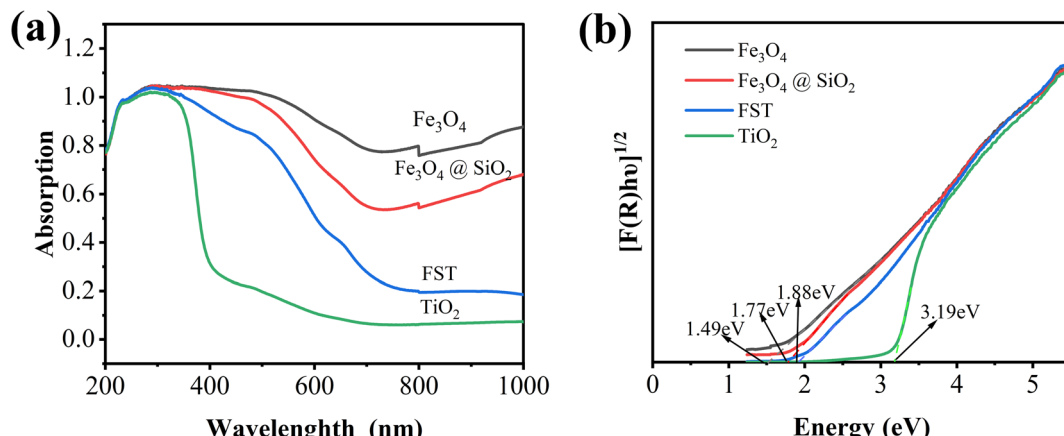


Fig. 3 (a) UV-vis diffuse reflectance spectrum (DRS), (b) Tauc plot of DRS.



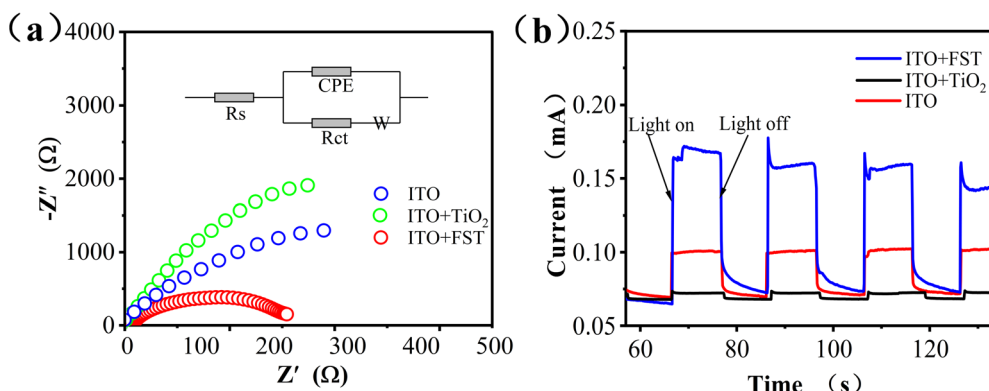


Fig. 4 (a) EIS responses of ITO, ITO + TiO<sub>2</sub> and ITO + FST, (b) surface photocurrent curves.

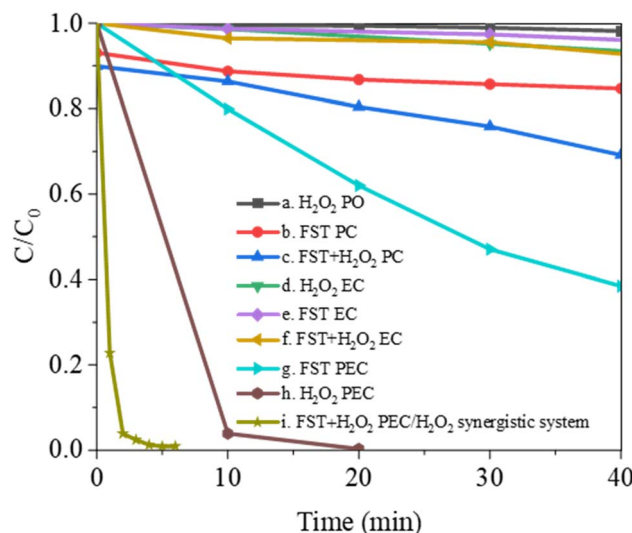


Fig. 5 MB degradation by photolysis (PO), photocatalysis (PC), electrocatalysis (EC), photoelectrocatalysis (PEC), and PEC/H<sub>2</sub>O<sub>2</sub> synergistic system.

PEC/H<sub>2</sub>O<sub>2</sub> synergistic system, anode potential was +0.6 V (vs. SCE). As shown in curve (a), the MB solution showed less than 1.9% degradation when irradiated with visible light in the H<sub>2</sub>O<sub>2</sub> PO for 40 min. Curve (b) showed that the degradation efficiency was slightly increased up to about 25% by visible-light PC after adding FST to the MB solution. Curve (c) represented the PC in the presence of H<sub>2</sub>O<sub>2</sub>, the degradation efficiency was significantly improved, and 31.1% of the MB was removed after 40 min. Curve (d-f) showed the experimental results under EC conditions. MB exhibited stability, whether H<sub>2</sub>O<sub>2</sub> (curve (d)) or FST (curve (e)) are added alone. After adding H<sub>2</sub>O<sub>2</sub> and FST at the same time (curve (f)), the removal rate slightly increased, while the degradation efficiency was less than 10% after 40 min. Curves (g) and (h) represented experimental results in PEC. Under these conditions, the removal rate of MB reached 61.5% after adding only FST for 40 min, the removal rate of MB reached 96.1% after adding only H<sub>2</sub>O<sub>2</sub> for 10 min, and was close to 100% after 20 min. Curve (i) showed the experimental results under PEC/H<sub>2</sub>O<sub>2</sub> synergistic degradation conditions. FST and

H<sub>2</sub>O<sub>2</sub> significantly improved MB degradation when they coexisted, the degradation efficiency was close to 100% after 5 min. Therefore, FST PEC has good synergistic effects with H<sub>2</sub>O<sub>2</sub> PO and can quickly remove pollutants.

The synergy factor (S) obtained from eqn (3)<sup>45</sup> elucidates on the synergy between PEC and H<sub>2</sub>O<sub>2</sub> photolysis in the PEC/H<sub>2</sub>O<sub>2</sub> degradation system, and demonstrates the priority of the combined process.

$$S = K_{12}/(K_1 + K_2) \quad (3)$$

where,  $K_1$ ,  $K_2$ , and  $K_{12}$  are kinetic constants for H<sub>2</sub>O<sub>2</sub> PO, PEC process, and PEC/H<sub>2</sub>O<sub>2</sub> synergistic system, respectively. Experimental data was fitted with the Langmuir-Hinshelwood model, and kinetic constants (Table 1) of the different degradation methods presented by the different curves (a, g, i) in Fig. 5 were calculated. Since the concentration of MB was low, it was assumed that the reaction would take place with a pseudo-first-order equation. The correlation coefficient ( $R^2$ ) for all processes was above 0.95, indicating that the assumption was reasonable. Based on Table 1, the kinetic constant  $K$  of the FST PEC/H<sub>2</sub>O<sub>2</sub> synergistic system ( $1.2924 \text{ min}^{-1}$ ) was found to be about 1436 and 53 times higher than that of the H<sub>2</sub>O<sub>2</sub> PO ( $0.0009 \text{ min}^{-1}$ ) and FST PEC ( $0.0244 \text{ min}^{-1}$ ), respectively. Substituting  $K_1$ ,  $K_2$  and  $K_{12}$  into eqn (3), the value of  $S$  was 51.08 (much greater than 1), indicating that the composite process was not a simple addition of PEC and H<sub>2</sub>O<sub>2</sub> photolysis.

### 3.4. Optimization of FST PEC/H<sub>2</sub>O<sub>2</sub> synergistic system

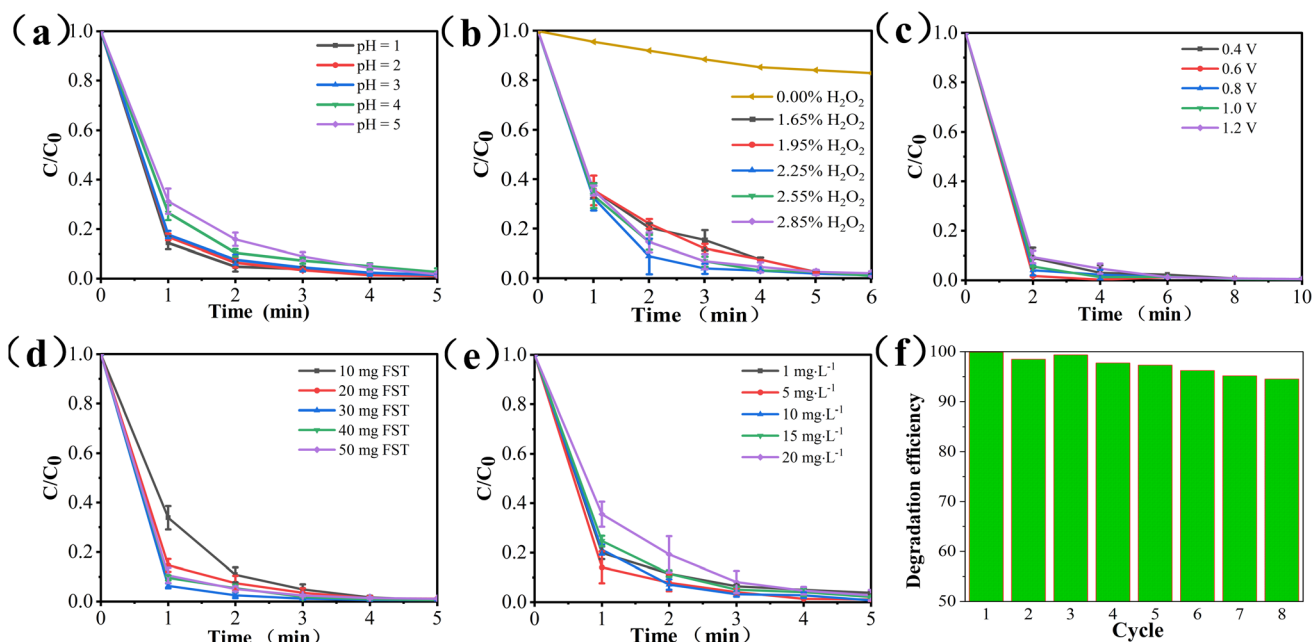
Using methylene blue (MB) as the model pollutant, the experimental conditions and degradation performance of the PEC/H<sub>2</sub>O<sub>2</sub> synergistic system was studied.

**Effects of pH.** To study the effects of the pH on MB degradation efficiency, the initial pH of the reaction solution, including  $10 \text{ mg L}^{-1}$  MB,  $0.05 \text{ mol per L}$  Na<sub>2</sub>SO<sub>4</sub>, and  $2.25\%$  H<sub>2</sub>O<sub>2</sub>, was adjusted to 1.0, 2.0, 3.0, 4.0, and 5.0, respectively, and the ITO + FST working electrode (fixed FST 30 mg) was applied at +0.6 V (vs. SCE) potential, after which degradation was performed by visible-light irradiation. MB degradation rates under different degradation times in each group were compared and analyzed (Fig. 6a). When pH was in the range of 1.0–5.0, the



Table 1 Kinetic constants and correlation coefficients ( $R^2$ ) of MB degradation

Curve in Fig. 5	Degradation system	Kinetic constant ( $\text{min}^{-1}$ )	$R^2$
a	$\text{H}_2\text{O}_2$ PO	0.0009 ( $K_1$ )	0.9620
g	FST PEC	0.0244 ( $K_2$ )	0.9979
i	FST + $\text{H}_2\text{O}_2$ PEC/ $\text{H}_2\text{O}_2$ synergistic system	1.2924 ( $K_{12}$ )	0.9562

Fig. 6 PEC/ $\text{H}_2\text{O}_2$  synergistic degradation of MB. (a) pH values, (b)  $\text{H}_2\text{O}_2$  concentration, (c) anodic potential, (d) FST fixation amount, (e) initial mass concentration of MB, (f) recycling test of FST.

degradation efficiency of MB reached 99% after 6 min. At the pH range of 1.0–3.0, the degradation efficiency was more than 80% after 1 min, and reduced to less than 80% at the pH range of 4.0–5.0, indicating that lower pH value is more conducive for improving photocatalytic activities.<sup>46</sup> The degradation efficiency was largest at pH 1.0, but its advantages relative to pH 2.0–3.0 were not marked. Therefore, pH 3.0 was selected as the optimal reaction pH value.

**Effects of  $\text{H}_2\text{O}_2$  concentrations.** To determine the impact of  $\text{H}_2\text{O}_2$  concentrations on PEC/ $\text{H}_2\text{O}_2$  synergistic degradation, the ITO + FST working electrode (fixed FST 30 mg) was applied at a bias voltage of +0.6 V (vs. SCE). The solution in the photocell contained 10 mg  $\text{L}^{-1}$  MB, 0.05 mol per L  $\text{Na}_2\text{SO}_4$ , and  $\text{H}_2\text{O}_2$  with concentrations of 0.00%, 1.65%, 1.95%, 2.25%, 2.55% and 2.85%, respectively. Finally, the solution was adjusted to pH value of 3.0. Degradation efficiency of MB at different degradation times under each group were compared and analyzed (Fig. 6b). The amount of  $\text{H}_2\text{O}_2$  was established to be an important factor in MB degradation. When  $\text{H}_2\text{O}_2$  concentration was 2.25%, degradation efficiency was highest within 1 to 3 min.  $\text{H}_2\text{O}_2$  is beneficial for photocatalytic reaction by trapping the conduction band  $e^-$  in order to generate more  $\cdot\text{OH}$  radicals.<sup>47</sup> However, when the concentration of  $\text{H}_2\text{O}_2$  was higher

than 2.25%, the degradation efficiency of MB didn't continue to increase (2.55%  $\text{H}_2\text{O}_2$ ), but decreased (2.85%  $\text{H}_2\text{O}_2$ ). Excess  $\text{H}_2\text{O}_2$  consumes  $\cdot\text{OH}$ , the main active species for degrading MB, and  $\text{H}_2\text{O}_2$  reacts with  $\cdot\text{OH}$  to generate  $\cdot\text{HO}_2$  or  $\cdot\text{O}_2^-$  with much less reactivity,<sup>48</sup> which reduces the catalytic reaction rate and is unfavorable for MB degradation. Therefore, the optimal concentration of  $\text{H}_2\text{O}_2$  in this system is 2.25%.

**Effects of applied anodic potential.** To examine the effects of various W.E. anodic potentials on degradation of MB, 10 mg  $\text{L}^{-1}$  MB, 0.05 mol per L  $\text{Na}_2\text{SO}_4$ , and 2.25%  $\text{H}_2\text{O}_2$  were added to the photoelectric reaction cell, the solution pH was adjusted to 3.0, and ITO + FST W.E. (fixed FST 30 mg) was applied at potentials of +0.4 V, +0.6 V, +0.8 V, +1.0 V, and +1.2 V (vs. SCE). As shown in Fig. 6c, MB rapidly degraded with increasing potential at the potential range of +0.4–+0.6 V (vs. SCE). At the potential of +0.6 V (vs. SCE), the degradation efficiency of MB was 98.25% within 2 min. The bias voltage applied on W.E. makes the visible-light photogenerated electrons to flow to the C.E. along the external circuit, thereby reacting with  $\text{H}_2\text{O}_2$  to generate  $\cdot\text{OH}$ .<sup>49</sup> However, as the potential continued to rise, degradation efficiency of MB decreased, because too high potential caused the electropolymerization of MB<sup>50</sup> and the oxidation of  $\text{H}_2\text{O}_2$ .  $\text{H}_2\text{O}_2$  had an oxidation peak at +0.6 V (vs. SCE) (Fig. S4†). If the



potential exceeded + 0.6 V, the  $\text{H}_2\text{O}_2$  added in the system was consumed by oxidation, which reduced the MB's degradation efficiency. Thus, anode potential +0.6 V (vs. SCE) is the optimal potential of the system.

**Effects of FST loading amounts.** The fixed amount of FST catalyst on the working electrode directly affects the degradation efficiency of MB. As displayed in Fig. 6d, the effects of FST loading amounts on MB degradation, where the conditions included  $10 \text{ mg L}^{-1}$  MB, 0.05 mol per L  $\text{Na}_2\text{SO}_4$ , 2.25%  $\text{H}_2\text{O}_2$ , pH 3.0, +0.6 V (vs. SCE) to the W.E. and different FST fixed quantities (10, 20, 30, 40, and 50 mg). When the fixed amounts of FST were 10–30 mg, the degradation efficiency of MB increased with increasing fixed amounts of catalysts. When the fixed amount of catalysts was 30 mg, the MB degradation efficiency was maximum, while the degradation efficiency of MB gradually decreased at >30 mg. Too much catalysts negatively affect the degradation efficiency, while agglomeration between catalyst particles reduces the number of active sites.<sup>51</sup> Besides, too much FST increases the thickness of the catalyst layer on the surface of ITO, which affects photoanode conductivity and visible light transmittance. Thus, the optimal fixed amount of FST is determined to be 30 mg.

**Effects of MB initial mass concentrations.** The effects of MB initial mass concentrations ( $1, 5, 10, 15, 20 \text{ mg L}^{-1}$ ) on degradation rates were evaluated. The system contained 0.05 mol per L  $\text{Na}_2\text{SO}_4$ , 2.25%  $\text{H}_2\text{O}_2$ , pH 3.0, the W.E. (fixed FST 30 mg) applied at the potential of +0.6 V (vs. SCE). The effects of initial mass concentration of MB solution on degradation were shown in Fig. 6e. The degradation efficiencies of five different concentrations of MB by FST PEC/ $\text{H}_2\text{O}_2$  system were above 90%, with  $10 \text{ mg L}^{-1}$  exhibiting the best degradation effect.

**Recyclability performance of FST.** The PEC/ $\text{H}_2\text{O}_2$  degradation experiment was performed at optimal conditions of  $10 \text{ mg L}^{-1}$  MB, 0.05 mol per L  $\text{Na}_2\text{SO}_4$ , 2.25%  $\text{H}_2\text{O}_2$ , pH 3.0, and +0.6 V (vs. SCE) potential to the W.E. (fixed FST 30 mg). After W.E. was vacuum-dried at 80 °C, the above degradation experiment was repeated 8 times, and then the degradation efficiency of MB measured each time. As can be seen from Fig. 6f, the MB degradation efficiency were above 98% within 5 recycled and reused experiments, and the degradation efficiency only showed a slight decrease in 6–8 degradation cycles, demonstrating that FST catalysts were recyclable and stable. Comparable findings have been reported, where such magnetically attached FST working electrode had the desired stability.<sup>53</sup> The magnetic FST was loaded on the surface of ITO working electrode by attractive forces of the magnet, the FST was firmly fixed and had a good stability.

### 3.5. PEC/ $\text{H}_2\text{O}_2$ synergistic degradation of pollutants

To further discussion the versatility of PEC/ $\text{H}_2\text{O}_2$  synergistic system for the treatment of different organic pollutants, the degradation experiments of four kinds of pollutants (MB, Rh B, MO, AMX) were carried out. As displayed in Fig. 7, the maximum degradation efficiencies of MB, Rh B, MO, and AMX in the FST PEC/ $\text{H}_2\text{O}_2$  synergistic system could reach up to 98.8%, 96.7%, 97.7% and 83.9% after 8 min illumination,

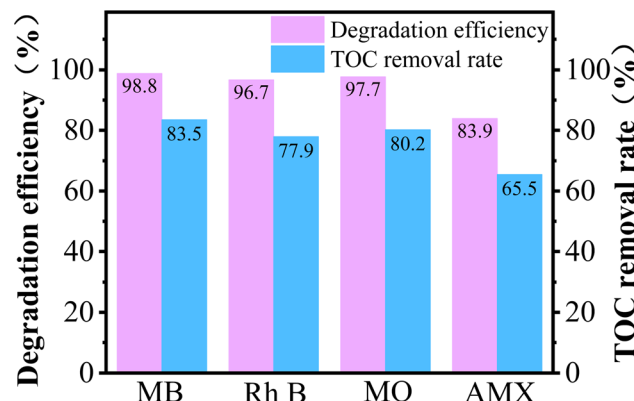


Fig. 7 Degradation efficiency and TOC removal rate of MB, Rh B, MO, and AMX.

respectively. Moreover, this system obtained TOC removal rate of 83.5% (MB), 77.9% (Rh B), 80.2% (MO), and 65.5% (AMX), indicating the incomplete mineralization of MB, Rh B, MO, and AMX in the PEC/ $\text{H}_2\text{O}_2$  system within 8 min and the presence of intermediate products. In general, the FST PEC/ $\text{H}_2\text{O}_2$  synergistic degradation system showed excellent oxidative degradation and mineralization abilities for MB, Rh B, MO, and AMX, indicating the wide applicability of PEC/ $\text{H}_2\text{O}_2$  coupling system for organic pollutants wastewater treatment.

### 3.6. Degradation mechanism

The possible reaction mechanism of the FST PEC/ $\text{H}_2\text{O}_2$  synergistic degradation system is shown in Fig. 8. When visible light irradiates FST, the energy ( $h\nu$ ) of the incident photon is higher than the semiconductor band gap ( $E_g$ ), and the electrons in the valence band (VB) are excited to transition into the conduction band (CB) to become highly active photogenerated electrons ( $e^-$ ); photogenerated positively charged holes ( $h^+$ ) stay in the VB, generating photogenerated  $h^+e^-$  pairs. Upon separation, the  $e^-$  and  $h^+$  move to the surface of the semiconductor. The  $h^+$  in the VB reacts with  $\text{H}_2\text{O}$  to generate hydroxyl radicals (eqn (4)); the  $e^-$  in the CB moves to the platinum counter electrode through an external circuit under the action of a bias voltage. Photogenerated  $e^-$  reacts with adsorbed or dissolved  $\text{O}_2$  on the electrode surface to form  $\cdot\text{O}_2^-$  (eqn (5)). In an acidic environment of the system,  $e^-$  reacts with  $\text{O}_2$  to form  $\text{H}_2\text{O}_2$  (eqn (6)),<sup>52,53</sup> after which  $\text{H}_2\text{O}_2$  reacts with  $\cdot\text{O}_2^-$  to produce more  $\cdot\text{OH}$  (eqn (7)).<sup>54</sup> By adding  $\text{H}_2\text{O}_2$  to the system,  $e^-$  can directly activate  $\text{H}_2\text{O}_2$  to generate a large number of  $\cdot\text{OH}$  (eqn (8)).<sup>49</sup> The  $\cdot\text{OH}$  and  $\cdot\text{O}_2^-$  in the system are involved in oxidative degradation of pollutants.



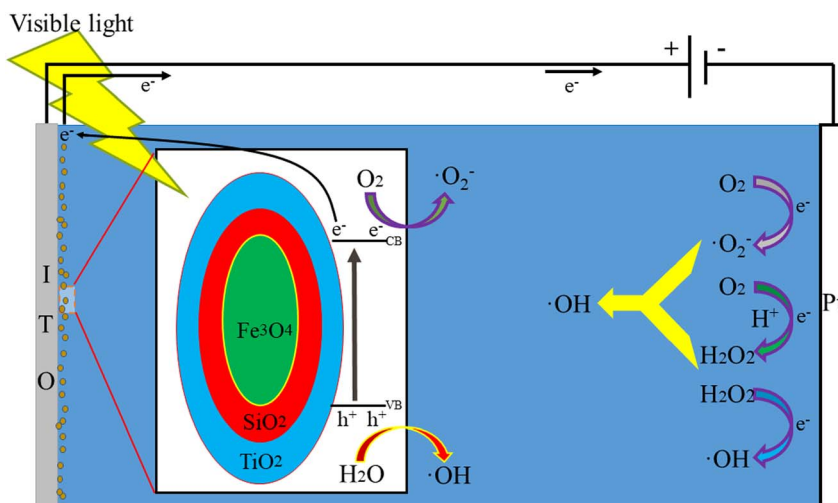


Fig. 8 Reaction mechanism of FST PEC/H<sub>2</sub>O<sub>2</sub> synergistic degradation system.



The free radical quenching experiment was performed to verify the generation and degradation mechanisms of active free radicals in the PEC/H<sub>2</sub>O<sub>2</sub> synergistic degradation reaction. Tert-butanol (TBA), benzoquinone (BQ), ethylenediaminetetraacetic acid disodium salt (EDTA-2Na), and silver nitrate (AgNO<sub>3</sub>) were respectively added to the FST PEC/H<sub>2</sub>O<sub>2</sub> degradation system for MB as quenchers, to scavenge for related reactive species, including hydroxyl radicals (·OH), superoxide radicals (·O<sub>2</sub><sup>·</sup>), photogenerated holes (h<sup>+</sup>) and photogenerated electrons (e<sup>-</sup>).<sup>55,56</sup> Fig. 9 displayed that addition of TBA, as a scavenger for ·OH, significantly inhibited the MB degradation reaction, indicating that ·OH was the main species in this system. From the eqn (4), (5), (6), (7) and (8), ·OH is the most active substance produced by the system. The degradation efficiency of MB slightly decreased after adding BQ, suggesting that variations of ·O<sub>2</sub><sup>·</sup> had little effects on MB degradation. ·O<sub>2</sub><sup>·</sup> was only generated by eqn (5), and accounted for a small

amount of active species. The addition of EDTA-2Na had no significant effects on MB degradation. Although EDTA-2Na captures h<sup>+</sup> and reduces the ·OH generated in eqn (4), the capture of h<sup>+</sup> is more conducive to separating e<sup>-</sup> and h<sup>+</sup>, and the eqn (5), (6), (7) and (8) caused by photogenerated e<sup>-</sup> can still generate large amounts of hydroxyl radicals, which continue to degrade pollutants. When AgNO<sub>3</sub> was added as an e<sup>-</sup> scavenger, MB undergoed a certain degradation efficiency change, indicating that e<sup>-</sup> played one significant role in this system. Eqn (5), (6), (7) and (8) show that e<sup>-</sup> contributes to generation ·O<sub>2</sub><sup>·</sup> and ·OH. Based on the above findings, the ·OH generated by e<sup>-</sup> and external H<sub>2</sub>O<sub>2</sub> in eqn (8) are the most important active species in the pollutant degradation process. In the FST PEC/H<sub>2</sub>O<sub>2</sub> synergistic degradation system, electrons are generated by FST photocatalysis, and bias voltage promotes separation of h<sup>+</sup> and e<sup>-</sup>. Due to reactions involving photogenerated h<sup>+</sup> and e<sup>-</sup>, ·OH and ·O<sub>2</sub><sup>·</sup> are formed, while electrons promote the formation of ·OH from a large amount of H<sub>2</sub>O<sub>2</sub> in the solution, forming the photocatalytic-electro-H<sub>2</sub>O<sub>2</sub> synergistic system to promote the rapid degradation of pollutants.

#### 4. Conclusions

In summary, visible-light driven PEC/H<sub>2</sub>O<sub>2</sub> coupling system was developed for degradation of organic pollutants (MB, Rh B, MO, AMX) by magnetic FST-loaded photoelectrode. Through characterization by TEM, XRD, UV-vis DRS, BET, XPS and EIS, the chemical and physical properties of the FST catalyst were systematically analyzed. Taking advantage of the synergistic effect of photoelectrocatalysis and H<sub>2</sub>O<sub>2</sub> photolysis, the system exhibited greatly enhanced performance. The FST PEC/H<sub>2</sub>O<sub>2</sub> synergistic degradation system showed comparable degradation efficiencies for MB (98.8%), Rh B (96.7%), MO (97.7%), and AMX (83.9%), indicating the wide applicability for various organic pollutants wastewater treatment. In the PEC/H<sub>2</sub>O<sub>2</sub> process, through applications of a bias voltage on the working electrode, photogenerated electrons were guided along the

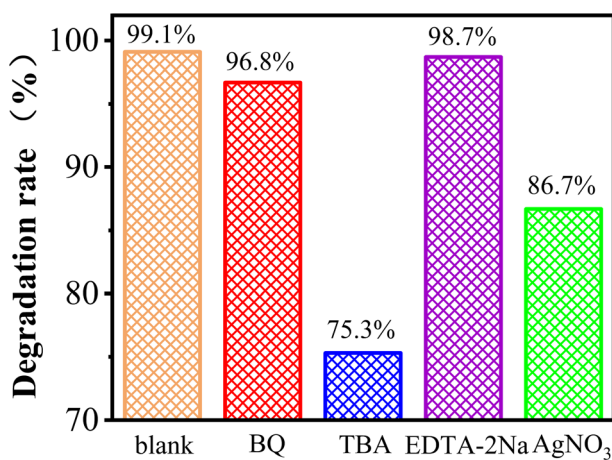


Fig. 9 Degradation efficiency of MB using different radical scavengers.



external electric field to the auxiliary electrode, thereby reducing  $h^+ - e^-$  recombination, realizing the photo-electric coupling effect. At the same time, the photogenerated electrons were captured by a sufficient amount of  $H_2O_2$  in the system to generate  $\cdot OH$ , which increased the amounts of strong oxidizing substances and facilitated the separation of photogenerated  $h^+$  and  $e^-$ . The results of quenching experiments also proved that  $\cdot OH$  and  $\cdot O_2^-$  were main reactive species in the photocatalytic-electro- $H_2O_2$  oxidation processes. This work brings new insights to efficiently purify organic pollutants by PEC coupled with peroxide under visible light illumination.

## Author contributions

Bo Zhang: investigation, methodology, writing – original draft. Xuemei Li: conceptualization, validation, resources, writing – review & editing, supervision, project administration, funding acquisition. Yongshan Ma: software, visualization. Tianyi Jiang: data curation. Yanyan Zhu: validation. Huixue Ren: supervision, funding acquisition. All authors have approved the final version of the manuscript.

## Conflicts of interest

There are no conflicts to declare.

## Acknowledgements

This project was financially supported by Natural Science Foundation of Shandong Province (No. ZR2020MD115, ZR2020MB086, ZR202102280483).

## References

- E. Bailón-García, A. Elmouwahidi, M. A. Álvarez, F. Carrasco-Marín, A. F. Pérez-Cadenas and F. J. Maldonado-Hódar, New carbon xerogel-TiO<sub>2</sub> composites with high performance as visible-light photocatalysts for dye mineralization, *Appl. Catal., B*, 2017, **201**, 29–40.
- P. An, Y. Fu, D. L. Wei, Y. L. Guo, W. C. Zhan and J. S. Zhang, Hollow Nitrogen-Rich Carbon Nanoworms with High Activity for Metal-Free Selective Aerobic Oxidation of Benzyl Alcohol, *Acta Phys.-Chim. Sin.*, 2021, **37**, 2001025.
- S. Li, W. Xu, L. Meng, W. Tian and L. Li, Recent Progress on Semiconductor Heterojunction-Based Photoanodes for Photoelectrochemical Water Splitting, *Small Sci.*, 2022, **2**, 2100112.
- Y. Zhang, S. M. Zhao, Q. W. Su and J. L. Xu, Visible light response ZnO-C<sub>3</sub>N<sub>4</sub> thin film photocatalyst, *Rare Met.*, 2021, **40**, 96–104.
- M. Xiao, Y. Qi, Q. Feng, K. Li, K. Fan, T. Huang, P. Qu, H. Gai and H. Song, P-cresol degradation through Fe(III)-EDDS/H<sub>2</sub>O<sub>2</sub> Fenton-like reaction enhanced by manganese ion: Effect of pH and reaction mechanism, *Chemosphere*, 2021, **269**, 129436.
- S. Qu, W. Wang, X. Pan and C. Li, Improving the Fenton catalytic performance of FeOCl using an electron mediator, *J. Hazard. Mater.*, 2020, **384**, 121494.
- I. Sirés, C. Arias, P. L. Cabot, F. Centellas, J. A. Garrido, R. M. Rodríguez and E. Brillas, Degradation of clofibric acid in acidic aqueous medium by electro-Fenton and photoelectro-Fenton, *Chemosphere*, 2007, **66**, 1660–1669.
- S. Periyasamy, X. Lin, S. O. Ganiyu, S. Kamaraj, A. Thiam and D. Liu, Insight into BDD electrochemical oxidation of florfenicol in water: kinetics, reaction mechanism, and toxicity, *Chemosphere*, 2022, **288**, 132433.
- R. Wang, J. Bai, Y. Li, Q. Zeng, J. Li and B. Zhou, BiVO<sub>4</sub>/TiO<sub>2</sub>(N<sub>2</sub>) Nanotubes Heterojunction Photoanode for Highly Efficient Photoelectrocatalytic Applications, *Nano-Micro Lett.*, 2016, **9**, 14.
- S. Wu and Y. H. Hu, A comprehensive review on catalysts for electrocatalytic and photoelectrocatalytic degradation of antibiotics, *Chem. Eng. J.*, 2021, **409**, 127739.
- P. Alulema-Pullupaxi, P. J. Espinoza-Montero, C. Sigchappallo, R. Vargas and J. L. Paz, Fundamentals and Applications of Photoelectrocatalysis as an Efficient Process to Remove Pollutants from Water: A Review, *Chemosphere*, 2021, **281**, 130821.
- J. Schneider, M. Matsuoka, M. Takeuchi, J. Zhang, Y. Horiuchi, M. Anpo and D. W. Bahnemann, Understanding TiO<sub>2</sub> photocatalysis: mechanisms and materials, *Chem. Rev.*, 2014, **114**, 9919–9986.
- Y. Z. Wang, M. Zu, X. S. Zhou, H. Lin, F. Peng and S. Q. Zhang, Designing efficient TiO<sub>2</sub>-based photoelectrocatalysis systems for chemical engineering and sensing, *Chem. Eng. J.*, 2020, **381**, 122605.
- Y. Li, D. D. Cheng, Y. Luo and L. X. Yang, Coaxial Fe<sub>2</sub>O<sub>3</sub>/TiO<sub>2</sub> nanotubes for enhanced photo-Fenton degradation of electron-deficient organic contaminant, *Rare Met.*, 2021, **40**, 3543–3553.
- C. Zhai, M. Zhu, Y. Lu, F. Ren, C. Wang, Y. Du and P. Yang, Reduced graphene oxide modified highly ordered TiO<sub>2</sub> nanotube arrays photoelectrode with enhanced photoelectrocatalytic performance under visible-light irradiation, *Phys. Chem. Chem. Phys.*, 2014, **16**, 14800–14807.
- Z. Q. Long, Q. G. Li, T. Wei, G. M. Zhang and Z. J. Ren, Historical development and prospects of photocatalysts for pollutant removal in water, *J. Hazard. Mater.*, 2020, **395**, 122599.
- G. Mamba and A. Mishra, Advances in Magnetically Separable Photocatalysts: Smart, Recyclable Materials for Water Pollution Mitigation, *Catalysts*, 2016, **6**, 79.
- W. J. Zhou, X. R. Xiao, Y. H. Liu and X. Zhang, Magnetic Se/Fe/PCN-Catalyzed Oxidative Cracking Alkenes in O<sub>2</sub>, *Chin. J. Org. Chem.*, 2022, **42**, 1849–1855.
- X. Y. Chen, J. F. Mao, C. Liu, C. Chen, H. E. Cao and L. Yu, An unexpected generation of magnetically separable Se/Fe<sub>3</sub>O<sub>4</sub> for catalytic degradation of polyene contaminants with molecular oxygen, *Chin. Chem. Lett.*, 2020, **31**, 3205–3208.
- D. Beydoun, R. Amal, G. Low and S. Mcevoy, Occurrence and prevention of photodissolution at the phase junction of



magnetite and titanium dioxide, *J. Mol. Catal. A: Chem.*, 2002, **180**, 193–200.

21 S. Xu, W. Shangguan, J. Yuan, M. Chen and J. Shi, Preparations and photocatalytic properties of magnetically separable nitrogen-doped  $\text{TiO}_2$  supported on nickel ferrite, *Appl. Catal., B*, 2007, **71**, 177–184.

22 P. M. Álvarez, J. Jaramillo, F. L. Ero and P. K. Plucinski, Preparation and characterization of magnetic  $\text{TiO}_2$  nanoparticles and their utilization for the degradation of emerging pollutants in water, *Appl. Catal., B*, 2010, **100**, 338–345.

23 Y. Chi, Q. Yuan, Y. Li, L. Zhao and W. Yan, Magnetically separable  $\text{Fe}_3\text{O}_4@\text{SiO}_2@\text{TiO}_2$ -Ag microspheres with well-designed nanostructure and enhanced photocatalytic activity, *J. Hazard. Mater.*, 2013, **262**, 404–411.

24 C. Feng, Y. Xie, J. Zhao and G. Lu, Photocatalytic degradation of dyes on a magnetically separated photocatalyst under visible and UV irradiation, *Chemosphere*, 2001, **44**, 1159–1168.

25 S. Kamaruddin and D. Stephan, The preparation of silica-titania core-shell particles and their impact as an alternative material to pure nano-titania photocatalysts, *Catal. Today*, 2011, **161**, 53–58.

26 I. Kitsou, P. Panagopoulos, T. Maggos, M. Arkas and A. Tsetsekou, Development of  $\text{SiO}_2@\text{TiO}_2$  core-shell nanospheres for catalytic applications, *Appl. Surf. Sci.*, 2018, **441**, 223–231.

27 M. Khan, C. S. L. Fung, A. Kumar, J. He and I. M. C. Lo, Unravelling mechanistic reasons for differences in performance of different Ti- and Bi-based magnetic photocatalysts in photocatalytic degradation of PPCPs, *Sci. Total Environ.*, 2019, **686**, 878–887.

28 A. Kumar, M. Khan, L. Fang and I. M. C. Lo, Visible-light-driven  $\text{N-TiO}_2@\text{SiO}_2@\text{Fe}_3\text{O}_4$  magnetic nanophotocatalysts: synthesis, characterization, and photocatalytic degradation of PPCPs, *J. Hazard. Mater.*, 2017, **370**, 108–116.

29 J. He, X. Zeng, S. Lan and I. M. C. Lo, Reusable magnetic  $\text{Ag}/\text{Fe}_3\text{O}_4@\text{SiO}_2$  composite for simultaneous photocatalytic disinfection of *E. coli* and degradation of bisphenol A in sewage under visible light, *Chemosphere*, 2018, **217**, 869–878.

30 Q. Y. Li, K. R. Ma, Z. J. Ma, Q. Wei, J. G. Liu, S. P. Cui and Z. R. Nie, Preparation and enhanced photocatalytic performance of a novel photocatalyst: hollow network  $\text{Fe}_3\text{O}_4$ /mesoporous  $\text{SiO}_2/\text{TiO}_2$  (FST) composite microspheres, *Microporous Mesoporous Mater.*, 2018, **265**, 18–25.

31 J. B. Cai, X. F. Lin and H. F. Zhou, Lysine surface modified  $\text{Fe}_3\text{O}_4@\text{SiO}_2@\text{TiO}_2$  microspheres-based preconcentration and photocatalysis for in situ selective determination of nanomolar dissolved organic and inorganic phosphorus in seawater, *Sens. Actuators, B*, 2016, **224**, 48–54.

32 J. Rashid, M. A. Barakat, Y. Ruzmanova and A. Chianese,  $\text{Fe}_3\text{O}_4@\text{SiO}_2@\text{TiO}_2$  nanoparticles for photocatalytic degradation of 2-chlorophenol in simulated wastewater, *Environ. Sci. Pollut. Res.*, 2015, **22**, 3149–3157.

33 J. Ma, S. Guo, X. Guo and H. G. Ge, Liquid-phase deposition of  $\text{TiO}_2$  nanoparticles on core-shell  $\text{Fe}_3\text{O}_4@\text{SiO}_2$  spheres: preparation, characterization, and photocatalytic activity, *J. Nanopart. Res.*, 2015, **17**, 1–11.

34 X. Hu, J. Yang and J. Zhang, Magnetic loading of  $\text{TiO}_2/\text{SiO}_2/\text{Fe}_3\text{O}_4$  nanoparticles on electrode surface for photoelectrocatalytic degradation of diclofenac, *J. Hazard. Mater.*, 2011, **196**, 220–227.

35 J. Su, Y. Zhang, S. Xu, S. Wang, H. Ding and S. Pan, Highly efficient and recyclable triple-shelled  $\text{Ag}@\text{Fe}_3\text{O}_4@\text{SiO}_2@\text{TiO}_2$  photocatalysts for degradation of organic pollutants and reduction of hexavalent chromium ions, *Nanoscale*, 2014, **6**, 5181–5192.

36 L. Zhang, W. Wang, S. Sun, Y. Sun, E. Gao and Z. Zhang, Elimination of BPA endocrine disruptor by magnetic  $\text{BiOBr}@\text{SiO}_2@\text{Fe}_3\text{O}_4$  photocatalyst, *Appl. Catal., B*, 2014, **148–149**, 164–169.

37 K. Bezerra, T. R. Fiaschitello, G. Labuto, H. S. Freeman and S. Costa, Reuse of water from real reactive monochromic and trichromic wastewater for new cotton dyes after efficient treatment using  $\text{H}_2\text{O}_2$  catalyzed by UV light, *J. Environ. Chem. Eng.*, 2021, **9**, 105731.

38 X. Li, S. Liu, D. Cao, R. Mao and X. Zhao, Synergetic activation of  $\text{H}_2\text{O}_2$  by photo-generated electrons and cathodic Fenton reaction for enhanced self-driven photoelectrocatalytic degradation of organic pollutants, *Appl. Catal., B*, 2018, **235**, 1–8.

39 P. D. R. A. Paula, R. P. Cavalcante, D. A. Da Silva, L. Silva, T. Silva, F. Gozzi, E. McGlynn, A. Brady-Boyd, G. A. Casagrande and H. Wender,  $\text{H}_2\text{O}_2$ -assisted photoelectrocatalytic degradation of Mitoxantrone using  $\text{CuO}$  nanostructured films: Identification of by-products and toxicity, *Sci. Total Environ.*, 2019, **651**, 2845–2856.

40 J. Sun, Y. Guo, Y. Wang and D. Cao,  $\text{H}_2\text{O}_2$  assisted photoelectrocatalytic degradation of diclofenac sodium at  $\text{g-C}_3\text{N}_4/\text{BiVO}_4$  photoanode under visible light irradiation, *Chem. Eng. J.*, 2018, **332**, 312–320.

41 Z. Lei, X. Pang, N. Li, L. Lin and Y. Li, A novel two-step modifying process for preparation of chitosan-coated  $\text{Fe}_3\text{O}_4/\text{SiO}_2$  microspheres, *J. Mater. Process. Technol.*, 2009, **209**, 3218–3225.

42 Q. Zhang, J. B. Joo, Z. Lu and M. Dahl, Self-assembly and photocatalysis of mesoporous  $\text{TiO}_2$  nanocrystal clusters, *Nano Res.*, 2011, **4**, 103–114.

43 Y. Ma, J. Cui, M. Yin, X. Li and Y. Liu, Enhancement of visible light driven dye degradation and photocatalytic  $\text{H}_2$  evolution over  $\text{MoS}_2$  through combination with perylene diimide aggregates, *New J. Chem.*, 2021, **45**, 14432–14443.

44 S. Komtchou, A. Dirany, P. Drogui, D. Robert and P. Lafrance, Removal of atrazine and its by-products from water using electrochemical advanced oxidation processes, *Water Res.*, 2017, **125**, 91–103.

45 P. Qiu, T. Zhao, X. Zhu, B. Thokchom, J. Yang, W. Jiang, L. Wang, Y. Fan, X. Li and W. Luo, A confined micro-reactor with a movable  $\text{Fe}_3\text{O}_4$  core and a mesoporous  $\text{TiO}_2$  shell for a photocatalytic Fenton-like degradation of bisphenol A, *Chin. Chem. Lett.*, 2021, **32**, 1456–1461.



46 A. Li, G. Li, Y. Zheng, L. Feng and Y. Zheng, Photocatalytic Property and Reaction Mechanism of (Ni-Mo)/TiO<sub>2</sub> Nano Thin Film Evaluated with Congo Red, *Acta Phys.-Chim. Sin.*, 2012, **28**, 457–464.

47 M. R. Sohrabi and M. Ghavami, Comparison of direct yellow 12 dye degradation efficiency using UV/semiconductor and UV/H<sub>2</sub>O<sub>2</sub>/semiconductor systems, *Desalination*, 2010, **252**, 157–162.

48 J. Ma, W. Song, C. Chen, W. Ma, J. Zhao and Y. Tang, Fenton Degradation of Organic Compounds Promoted by Dyes under Visible Irradiation, *Environ. Sci. Technol.*, 2005, **39**, 5810–5815.

49 R. Daghrir, P. Drogui and M. A. El Khakani, Photoelectrocatalytic oxidation of chlortetracycline using Ti/TiO<sub>2</sub> photo-anode with simultaneous H<sub>2</sub>O<sub>2</sub> production, *Electrochim. Acta*, 2013, **87**, 18–31.

50 J. Xu, H. Olvera-Vargas, F. Y. H. Teo and O. Lefebvre, A comparison of visible-light photocatalysts for solar photoelectrocatalysis coupled to solar photoelectro-Fenton: application to the degradation of the pesticide simazine, *Chemosphere*, 2021, **276**, 130138.

51 A. Sharma and B. Lee, Integrated ternary nanocomposite of TiO<sub>2</sub>/NiO/reduced graphene oxide as a visible light photocatalyst for efficient degradation of o-chlorophenol, *J. Environ. Manage.*, 2016, **181**, 563–573.

52 C. Qu and D. Liang, Novel electrochemical advanced oxidation processes with H<sub>2</sub>O<sub>2</sub> generation cathode for water treatment: a review, *J. Environ. Chem. Eng.*, 2022, **10**, 107896.

53 P. J. Espinoza-Montero, P. Alulema-Pullupaxi and B. A. Frontana-Uribe, Electrochemical production of hydrogen peroxide on Boron-Doped diamond (BDD) electrode, *Curr. Opin. Solid State Mater. Sci.*, 2022, **26**, 100988.

54 D. Liu, R. Tian, J. Wang, E. Nie, X. Piao, X. Li and Z. Sun, Photoelectrocatalytic degradation of methylene blue using F doped TiO<sub>2</sub> photoelectrode under visible light irradiation, *Chemosphere*, 2017, **185**, 574–581.

55 F. Chen, Q. Yang, Y. Wang, J. Zhao, D. Wang, X. Li, Z. Guo, H. Wang, Y. Deng, C. Niu and G. Zeng, Novel ternary heterojunction photocatalyst of Ag nanoparticles and g-C<sub>3</sub>N<sub>4</sub> nanosheets co-modified BiVO<sub>4</sub> for wider spectrum visible-light photocatalytic degradation of refractory pollutant, *Appl. Catal., B*, 2017, **205**, 133–147.

56 C. Zhou, C. Lai, D. Huang, G. Zeng, C. Zhang, M. Cheng, L. Hu, J. Wan, W. Xiong, M. Wen, X. Wen and L. Qin, Highly porous carbon nitride by supramolecular preassembly of monomers for photocatalytic removal of sulfamethazine under visible light driven, *Appl. Catal., B*, 2018, **220**, 202–210.

